

Microbial redox cycling enhances ecosystem thermodynamic efficiency and productivity

Mayumi Seto¹ and Michio Kondoh²

¹Nara Women's University

²Tohoku University

January 31, 2023

Abstract

Microbial life in an ecosystem with low energy supply has been considered to employ two energy utilization strategies. The first is energy conservation at an individual level, while the second is energy use optimization in response to the availability of energy resources. Here, using an oxidation-reduction (redox) reaction network model where microbial metabolic pathways are established through multiple species-level competition and cooperation within a redox reaction network, we hypothesize that microbial ecosystems can move forward to increase energy use efficiency, namely an energy efficiency strategy at the community level. This strategy is supported by microbial functional diversity that enables species to interact with others in various ways of metabolic handoffs. Moreover, the high energy use efficiency is attributable to the mutualistic division of labor that increases the complexity of metabolic pathways, which actively drives material cycling to exploit more energy.

1 **Microbial redox cycling enhances ecosystem thermodynamic efficiency and**
2 **productivity**

3 ^{a*}Mayumi Seto and ^{b*}Michio Kondoh

4 **Affiliations:**

5 ^a*Department of Chemistry, Biology, and Environmental Sciences, Nara Women's*
6 *University, Kita-Uoya Nishimachi, Nara 630-8506, Japan*
7 seto@ics.nara-wu.ac.jp

8 ^b*Graduate School of Life Sciences, Tohoku University, 6-3 Aramaki Aza Aoba, Aoba-ku,*
9 *Sendai 980-8578, Japan*

10 **Running Title:** Microbial redox cycling: Eco-redox model

11

12 **Keywords:**

13 division of labor, mutualism, community network, microbial ecology, population
14 dynamics, thermodynamics, niche construction, material cycle, redox chemistry,
15 biogeochemistry

16 **Type of Article:** Letter

17 **Data availability**

18 If the manuscript is accepted, data supporting the results will be archived in
19 Dryad and the data DOI will be included at the end of the article.

20 Furthermore, we provide all the information needed to replicate the
21 simulations in Supplemental Information. All codes were written in the Wolfram
22 Language platform using Mathematica 12. The codes are available in Example.nb. See
23 details in Section S2.2.

24

25 **Number of**

Words in the abstract	Words in the main text	References	Figures	Tables	Text boxes
140	4526	40	6	0	0

26

27 **Statement of authorship**

28 M.S and M.K conceived of the presented idea. M.S designed the model and
29 the computational framework and analyzed the data. M.S and M.K contributed equally
30 to the interpretation of the results and writing the manuscript.

31

32 **Abstract**

33 Microbial life in an ecosystem with low energy supply has been considered to
34 employ two energy utilization strategies. The first is energy conservation at an
35 individual level, while the second is energy use optimization in response to the
36 availability of energy resources. Here, using an oxidation-reduction (redox) reaction
37 network model where microbial metabolic pathways are established through multiple
38 species-level competition and cooperation within a redox reaction network, we
39 hypothesize that microbial ecosystems can move forward to increase energy use
40 efficiency, namely an energy efficiency strategy at the community level. This strategy is
41 supported by microbial functional diversity that enables species to interact with others
42 in various ways of metabolic handoffs. Moreover, the high energy use efficiency is
43 attributable to the mutualistic division of labor that increases the complexity of
44 metabolic pathways, which actively drives material cycling to exploit more energy.

45

46 **Introduction**

47 All life on Earth relies on ATP as the primary energy carrier, and its
48 production and transfer significantly depend on the ecosystems' electron transfer
49 potential. In the surface ecosystems, sunlight fuels electron transfer for ATP synthesis
50 via photosynthesis, following which aerobic respirators harvest chemical energy by
51 transferring electrons stored in organic carbon to oxygen in a redox reaction. Aerobic
52 respiration and various of redox reactions (e.g., denitrification, iron oxidation, and
53 methanogenesis) supply power to prokaryotic organisms. In particular, inorganic redox
54 reactions must have been the fundamental energy sources for life before the evolution of
55 photosynthesis. In the subsurface realm, which replicates the conditions of the early
56 Earth where organic carbon and oxygen were not readily available, the power available
57 for microbes is significantly limited compared with that in surface ecosystems (Momper
58 *et al.* 2017; Bradley *et al.* 2020). Nevertheless, the microbial biomass in the subsurface
59 today is several to tens of PgC (Kallmeyer *et al.* 2012; Bar-On *et al.* 2018; Magnabosco
60 *et al.* 2018), comprising nearly 70% of the overall microbial cells on Earth (Flemming
61 & Wuertz 2019). Thus, it remains a mystery as to how these microbial communities
62 maintain their productivity in energetically (or thermodynamically) less favorable
63 environments (Hoehler & Jørgensen 2013a; Starnawski *et al.* 2017).

64 One adaptive strategy for microorganisms harbored in such environments is
65 the conservation of energy at the individual level. Indeed, subsurface microorganisms
66 appear to minimize energy expense to maintain their vital functions until sufficient
67 energy for growth becomes available (Jørgensen & Boetius 2007; Morono *et al.* 2011;
68 Hoehler & Jørgensen 2013b). Another strategy is to optimize the energy exploitation in
69 response to the change in resource influx. Fermentation, the partial breakdown of

70 organic carbon, produces less ATP per organic carbon than that produced by aerobic
71 respiration, which involves the complete oxidation of organic carbon to carbon dioxide.
72 Although fermentation is thermodynamically less favorable than aerobic respiration,
73 fermentation can produce more ATP per time at higher organic carbon influx rates
74 owing to the trade-off between the yield and rate of ATP production (Pfeiffer *et al.*
75 2001; Kreft *et al.* 2020). Experimental, observational, and metagenomic evidence
76 supports that microbes often sequentially proceed with incomplete reactions that are
77 generally less thermodynamically favorable than a complete reaction wherein they
78 divide metabolic labor within the community by exchanging reaction byproducts
79 (excreted metabolites) or even electrons directly from one to another (McInerney *et al.*
80 2009; Morris *et al.* 2013; Embree *et al.* 2015; Kouzuma *et al.* 2015; Anantharaman *et*
81 *al.* 2016). This so-called division of metabolic labor also seems to be related to the
82 energy utilization efficiency of microbial communities. However, it is unclear whether
83 such a division of labor can be advantageous and increase energy utilization efficiency
84 at the community level within a redox network where various microbial reactions and
85 interactions are entangled with each other.

86 To address this question, we developed an eco-redox model, a microbial
87 community network model based on thermodynamic and redox properties. We found
88 that, without assuming a trade-off between the yield and rate of ATP production, species
89 that mutually divide the metabolic labor and enhance material cycling can replace species
90 harnessing energetically more favorable reactions. Thermodynamic calculations suggest

91 that a microbial community composed of a mutualistic division of labor is endowed with
92 higher energy utilization efficiency and productivity. Furthermore, we found that
93 microbial ecosystems with metabolic functional diversity can move forward to increase
94 the energy utilization efficiency and productivity.

95

96 **Methods**

97 **Eco-redox model**

98 We constructed a conceptual model that explicitly links population dynamics to
99 the redox process within the general framework of thermodynamics and redox
100 chemistry to build a theoretical foundation that integrates the dynamics of microbial
101 community and redox reaction network (Fig. 1). The electron fluxes in geochemical
102 cycles on Earth are mainly driven by the chemical substances of C, N, S, Fe, Mn, O, and
103 H (Falkowski *et al.* 2008). In our model, each chemical substance involving a redox
104 network was denoted by X_j , where X indicates a characteristic element ($X = A, B, C,$
105 \dots) and j is the relative number of electrons that X holds ($1 \leq j \leq N_X$). j is not exactly
106 equal to the actual oxidation state but shows the relative electron density; X_1 possesses
107 the lowest electron density within the X -bearing substances present in the system. For
108 instance, for nitrogen-bearing substances as an example, when X_1 is N_2 , NH_2OH , N_2H_4 ,
109 and NH_3 (or NH_4^+) can correspond to X_2 , X_3 , and X_4 , respectively. Assuming that no
110 chemical substances with the same oxidation state of X exists in a system and the half-
111 reaction $X_j + (z-j)e^- \rightleftharpoons X_z$ holds (where $j < z$ and e^- denotes an electron), a redox
112 network template was designed using all possible combinations of two half-reactions

113 (an oxidation reaction losing electrons and a reduction reaction gaining electrons) in the
 114 system (see Supporting Information Section S1). The topological structure of a redox
 115 network and the number of possible redox reactions forming the network (N_{redox}) were
 116 uniquely determined for a given N_{tot} chemical substances (Fig. 1a). Each of the smaller
 117 vertexes in Fig. 1a show a possible forward and backward redox reaction, which
 118 converts the given reactants into given products via edges (Fig. 1a). Although not all
 119 redox reactions in natural systems are confirmed to be utilized as microbial energy
 120 sources (Kuypers *et al.* 2018), all redox reactions forming the redox network template
 121 are assumed to be available for microbes to harness. In other words, the metabolic
 122 diversity of a community determines the complexity of the redox network template.

123 Within the network, the thermodynamic (energetic) advantage of a reaction was
 124 characterized in terms of the Gibbs energy utilized per reaction (Fig. 1b). The amount of
 125 Gibbs energy associated with the chemical substances of all X_j was defined as $G =$
 126 $V \sum [X_j] \mu_{X_j}$ where V , $[X_j]$, and μ_{X_j} denote the volume of the system (L), the molar
 127 concentration of X_j (mol L^{-1}), and the chemical potential of X_j (kJ mol^{-1}), respectively.

128 The negative value of the Gibbs energy change of the i th reaction ($-\Delta_r G_i$ [kJ mol^{-1}])
 129 designates the maximum energy supply per reactant available for a microbial cell to
 130 synthesize ATP. $-\Delta_r G_1$ for reaction 1 in Fig. 1a ($A_1 + C_2 \rightarrow A_2 + C_1$) is determined as
 131 follows:

132

$$\begin{aligned}
 133 \quad -\Delta_r G_1 &= \mu_{A_1} + \mu_{C_2} - \mu_{A_2} - \mu_{C_1} \\
 134 \quad &= -\Delta_r G_1^\circ + RT \ln \frac{[A_1][C_2]}{[A_2][C_1]}, \quad (1)
 \end{aligned}$$

135 where

$$136 \quad -\Delta_r G_1^\circ = \mu_{A_1}^\circ + \mu_{C_2}^\circ - \mu_{A_2}^\circ - \mu_{C_2}^\circ$$

137 $^\circ$ denotes the standard state at a specific temperature (15 °C), pressure (1 bar), and

138 concentration (1 mol L⁻¹); R and T are the gas constant and the absolute temperature,

139 respectively. The activity of X_j was replaced by the molar concentration in this study.

140 A group of species that utilize an identical redox reaction as an energy source is

141 hereafter referred to as a microbial species (Sp). We considered an open system where

142 as many microbial species as N_{reac} are introduced without additional exchange of cells

143 with the surroundings. The population dynamics of Sp i , which specifically harness

144 reaction i for population growth, were kinetically or thermodynamically limited

145 depending on the abundance of the reactants and the Gibbs energy:

146

$$147 \quad \frac{dM_i}{dt} = q_i(c_i(-\Delta_r G_i)f_i - m_i)M_i, \quad (2a)$$

148 where

$$149 \quad f_1 = r_1 \frac{[A_1]}{K_{1,A_1} + [A_1]} \frac{[C_2]}{K_{1,C_2} + [C_2]} \quad \text{for reaction 1 in Fig 1a.} \quad (2b)$$

150

151 M_i is the biomass of Sp i ; $-\Delta_r G_i$ (kJ mol⁻¹) is the $-\Delta_r G$ of the i th reaction; f_i is the

152 microbial catalytic rate of the i th reaction, where r_1 and K_{1,X_j} are respectively the

153 maximum catalytic rate per biomass (mol g⁻¹ h⁻¹) and the Michaelis–Menten constants

154 (mol L⁻¹); q_i is the biomass yield per energy (g kJ⁻¹); c_i is the fraction of energy that

155 can be used for ATP synthesis ($0 \leq c_i \leq 1$); and m_i is the maintenance energy of Sp i (kJ

156 $\text{g}^{-1} \text{h}^{-1}$) (Seto & Iwasa 2019a). For numerical simulations, the values of r_i and K_{i,X_j}
 157 were determined independently from the thermodynamic favorability of the i th reaction
 158 without assuming the trade-off between the yield and rate of ATP production. The
 159 dynamics of the molar concentration of $[X_j]$ were determined as follows:

160

$$161 \quad \frac{d[X_j]}{dt} = I_{X_j} - D_{X_j}[X_j] + \sum \alpha_{i,X_j} f_i M_i + \sum \alpha_{i,X_j} F_i, \quad (3)$$

162

163 where I_{X_j} and D_{X_j} are the inflow rate ($\text{mol L}^{-1} \text{h}^{-1}$) and the outflow rate constant (h^{-1}) of
 164 X_j , respectively. The third and fourth terms denote the microbial and abiotic reaction
 165 rates where α_{i,X_j} is the stoichiometric constant of X_j in reaction i . The abiotic reaction
 166 rate (F_i) is proportional to the product of the molar concentration of the reactant(s) with
 167 the reaction rate constant k_i . Under the given different thermodynamic or microbial
 168 parameters, different pathways can be established at the steady state within the same
 169 redox network template (Fig. 1c). Microbially driven material flows among X-bearing
 170 substances may incorporate cyclic structures, which may also consist of subcycles.

171

172 **Numerical simulations**

173 We developed an algorithm in the Wolfram language in Mathematica 12, which
 174 automatically formulates the list of redox reactions and simulates the dynamics of N_{reac}
 175 Sps and N_{tot} chemical substances, once the numbers of X-bearing substances, N_X , are
 176 determined (see section S2). Two scenarios for the inflow rate of X_j (I_{X_j}) were considered:
 177 (i) the inflow rates of all X_j were uniformly increased ($I_{X_j} = [\text{Inflow rate}]/N_{\text{tot}}$), and (ii)

178 the inflow rates of only the most oxidized electron acceptors X_1 were uniformly increased
179 ($I_{X_1} = [\text{Inflow rate}]$ and 10^{-5} for other X_j). The scenario (i) explores the redox
180 boundary system where both electron donors (X_j with larger j) and acceptors (X_j with
181 smaller j) are supplied at different levels in a well-balanced manner, whereas the scenario
182 (ii) investigates the transition from reduced to oxidized state, respectively. The redox
183 balance of the inflow was evaluated by determining the relative oxidation number of X_j
184 (E_{X_j}). The relative oxidation number of X_j with $j = 1$ was considered -1 and the relative
185 oxidation number of X_j for which j is the maximum value among all X_j (j_{max}) was
186 considered $+1$. The relative oxidation number of other X_j was determined as $E_{X_j} = -1$
187 $+ 2/(j_{max} - 1)$. The redox balance of the inflow is given by $\sum_X \sum_j E_{X_j} I_{X_j}$.

188 The initial conditions of variables, default values of parameters, and ranges for
189 random variables are summarized in Table S1. $N_{tot} = 6, 7, 8, 9, 10, 11,$ and 12 correspond
190 to $(N_A, N_B, N_C) = (2, 2, 2), (3, 2, 2), (3, 3, 2), (3, 3, 3), (4, 3, 3), (4, 4, 3),$ and $(4, 4, 4),$
191 respectively.

192

193 **Gibbs energy at the microbes-free state and equilibrium**

194 The thermodynamic efficiency of microbial community was evaluated by
195 comparing the Gibbs energy characterized by microbial community activity (G_{bio}), G at
196 the microbes-free state (G_{abio}), and the equilibrium G (G_{eq}). For a microbe-free open
197 system, the molar concentrations of X_j were determined using the balance of exchanges
198 of X_j with the surroundings and abiotic reaction rates. Because we only simulated the
199 case where the input and output rates of X_j (I_{X_j} and D_{X_j}) are at least a few orders of

200 magnitude higher than the abiotic reaction rate constants, the molar concentration of X_j
 201 can be approximated by I_{X_j}/D_{X_j} . The steady state Gibbs energy at the microbe-free state
 202 was determined as follows:

203

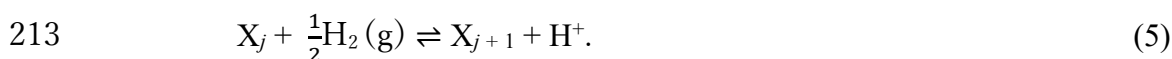
$$204 \quad G_{abio}^* = V \sum_X \sum_j \mu_{X_j} \frac{I_{X_j}}{D_{X_j}} = V \sum_X \sum_j \left(\mu_{X_j}^\circ + RT \ln \frac{I_{X_j}}{D_{X_j}} \right) \frac{I_{X_j}}{D_{X_j}}, \quad (4)$$

205

206 where * denotes a steady state.

207 The thermodynamic equilibrium refers to the state in which no further change
 208 occurs in an isolated system (i.e., $I_{X_j} = 0$ and $D_{X_j} = 0$ for all X_j) where all half-reactions
 209 comprising the redox network template must have reached equilibrium. For a half-
 210 reaction $X_j + e^- \rightarrow X_{j+1}$ ($1 \leq j \leq (N_X - 1)$), the redox reaction with a reference reaction
 211 ($1/2H_2(g) \rightarrow H^+ + e^-$) is as follows:

212



214

215 Because the standard chemical potentials of $H_2(g)$ and H^+ are 0, the standard Gibbs
 216 energy change of Eq. 4 is $\Delta_r G_j^\circ = \mu_{X_{j+1}}^\circ - \mu_{X_j}^\circ$. Letting the equilibrium constant of Eq.
 217 5 be K_j and solving $\Delta_r G_j = \Delta_r G_j^\circ + RT \ln K_j = 0$ for K_j ,

218

$$219 \quad K_j = \exp \left\{ -\frac{\Delta_r G_j^\circ}{RT} \right\}. \quad (6)$$

220

221 Using Eq. 6, the equilibrium molar concentration of X_j ($j \geq 2$) satisfies

222

223
$$K_j[\widehat{X_{j-1}}] = \prod_{i=1}^j K_i [\widehat{X_1}] \quad (7)$$

224

225 where the hat denotes the equilibrium. Letting T_X be the total number of moles of X-
226 bearing substances, which is conserved in the isolated system:

227

228
$$T_X = [X_1] + [X_2] + [X_3] + \dots + [X_{N_X}]$$

229
$$= [\widehat{X_1}] + K_1[\widehat{X_1}] + K_1K_2[\widehat{X_1}] + K_1K_2K_3[\widehat{X_1}] + \dots + [\widehat{X_1}] \prod_{i=1}^{N_X} K_i$$

230
$$= [\widehat{X_1}](1 + \sum_{j=1}^{N_X} \prod_{i=1}^j K_i) \quad (8)$$

231

232 Solving Eq. 8 for $[\widehat{X_1}]$,

233

234
$$[\widehat{X_1}] = \frac{T_X}{1 + \sum_{j=1}^{N_X} \prod_{i=1}^j K_i} \quad (9)$$

235

236 The molar concentrations of other X_j ($j \geq 2$) at equilibrium were obtained using Eq. 7.

237 The equilibrium Gibbs energy is

238

239
$$G_{eq} = V \sum_X \sum_j \mu_{X_j}[\widehat{X_j}] = V \sum_X \sum_j \left(\mu_{X_j}^\circ + RT \ln[\widehat{X_j}] \right) [\widehat{X_j}]. \quad (10)$$

240

241 For comparison, T_X and V were fixed to $\sum_j I_{X_j}/D_{X_j}$ for each X and 1, respectively.

242

243 **Results**

244 **Co-development of the division of labor and material cycling**

245 Analysis of the eco-redox model revealed that energetically less favorable
246 reactions can be intensively driven by the division of labor, which is closely linked to
247 the topological structure of microbial pathways, depending on metabolic handoffs,
248 energy allocation, and material cycling. For a template consisting of six reactions at
249 $(N_A, N_B, N_C) = (2, 2, 2)$, not only each Sp in Fig. 2a competes for the same reactant at
250 the species-level, but Sps 2 and 3 as an assembly unit also compete with Sp 1 because
251 the consortium of Sps 2 and 3 proceed with reaction 1 by recycling B₁ and B₂ as
252 electron carriers (Seto & Iwasa 2019b, 2020). Furthermore, Sps 2 and 3 are in a division
253 of labor to complete reaction 1 by allocating the available Gibbs energy per reaction to
254 each other. For a more complex redox network, the forms of division of labor are not
255 straightforward because multiple Sps split a reaction into several ones (e.g.,
256 segmentation of $A_1 \rightarrow A_4$ into $A_1 \rightarrow A_2$, $A_2 \rightarrow A_3$, and $A_3 \rightarrow A_4$) and a single Sp
257 participates in several reactions as a module (Fig. 2b). For such a system, the magnitude
258 of each $-\Delta_r G_i$ relative to the maximum $-\Delta_r G_i$ of all reactions, $\rho_i = -\Delta_r G_i / \max(-\Delta_r G_1,$
259 $\dots, -\Delta_r G_{N_{\text{reac}}})$, provides a measure of the degree of segmentation of the i th reaction
260 within the template. ρ_i also shows the dependency of Sp i on others as Sp i that uses a
261 reaction with significantly low ρ_i is unlikely to survive on its own.

262 In an ecological context, as each redox reaction can be regarded as a niche
263 whose relative potential quality is given by ρ_i , Sp i using a high-quality reaction seems
264 more likely to grow faster. However, despite the presence of reactions with larger ρ_i
265 within the template, Sps using reactions with surprisingly smaller ρ_i often survived and
266 consisted of pathways at a steady state (Fig. 2c). Under the given chemical and
267 microbial conditions in Fig. 2c, Sp 8 occupied the most energetically favorable reaction

268 niche, whereas Sps 6, 19, and 41 using extremely low-quality segmented reactions
269 survived at a steady state. Sps 19 and 41 were confirmed to even become extinct when
270 each of them solely invaded the microbe-free system. Such an unexpected survival of
271 Sps 19 and 41 can be deciphered by consecutively introducing each Sp out of the Sps
272 that survived at the steady state to the microbe-free system to examine how interspecific
273 interactions alter the reaction niches by connecting pathways (Fig. 2d). Although Sps 6,
274 19, and 41 negatively affect each other in terms of the utilization of C-bearing
275 substances, the presence of Sp 6 is not sufficient but essential for the survival of Sps 19
276 and 41. This is because Sp 6 is a key cog to complete the cycle of A, improving the
277 quality of the niches of Sps 19 and 41 by enhancing metabolic handoffs among A-
278 bearing substances. Although the population growth of Sp *i* generally decreases the
279 Gibbs energy of the system, the invasion of Sp *i* can improve other Sp's reaction niches
280 by increasing the $-\Delta_r G$ of other Sps' energy source reactions. In particular,
281 establishing a cyclic pathway tends to encourage the survival of Sp that uses a low-
282 quality reaction niche.

283 The number of cycles in the established pathways at a steady state increases in
284 response to the increase in the inflow of X_j when both electron acceptors and donors are
285 supplied, which are possible at redox boundaries in natural systems (Fig. 3a). The
286 excessive supply (or lack) of electrons depletes electron acceptors (or donors), during
287 which the cycles are less likely to be established (Fig. 3b and c). The results are
288 consistent with the observations at redox boundaries of natural aqueous systems or
289 sediments where the supply of both electron donors and acceptors facilitates microbial
290 material recycling and favors the growth of species that mutually operate those

291 reactions (Roden *et al.* 2004; Zerkle & Mikhail 2017). The increase in the number of
292 cycles is accompanied by an increase in the number of Sps survived and a decline in ρ_i
293 forming the established pathways. This suggests the facilitated division of labor into
294 smaller units, even without assuming the trade-off between the yield and rate of ATP
295 production (Fig. 3d). Hence, the supply of both electron donors and acceptors can
296 enhance the division of labor that drive material cycles within a redox network.

297 An Sp using a reaction with smaller ρ_i may seem to only benefit from others.
298 However, such Sp can play an essential role in the survival of the consortium that
299 competes for Sp monopolizing the energetically more favorable reaction (Fig. 2a and b).
300 For instance, the consortium of Sps 6, 19, 28, and 41 collectively proceed with $B_3 + C_2$
301 $\rightarrow B_2 + C_3$ (reaction 29), which outcompetes the Sp that exclusively harnesses reaction
302 29 and is more energetically favorable than segmented reactions. Such an entangling
303 interplay is a good illustration of the survival strategy of microbes that form
304 consortiums, whose growth would otherwise be thermodynamically limited (Bryant *et*
305 *al.* 1967; Hoehler *et al.* 1994; Boetius *et al.* 2000). The results also explain the difficulty
306 of isolating some species, especially chemolithoautotrophs harnessing reactions with
307 lower $-\Delta_rG$. This is because the survival of those species might entirely depend on the
308 co-presence of a key species that seems irrelevant and unhelpful but crucially supports
309 the survival of the target species by modifying the material flow.

310

311 **Predominance of the division of labor and thermodynamic efficiency**

312 The topological structure of a redox network template determines the possible
313 forms of division of labor. However, how do Sps with labor division confront Sps using

314 more energetically favorable reactions? The key strategy is to increase the
315 thermodynamic efficiency to use more Gibbs energy as an assembly unit, which
316 enhances ecosystem productivity. An illustrative example is a competition between Sps
317 within a redox network at $(N_A, N_B, N_C) = (2, 2, 2)$, where two Sps maximally survive.
318 These two are either competitive or mutualistic, whereas the latter Sps (mutualistic Sps)
319 also compete with the Sp monopolizing the complete reaction (monopoly Sp; see Fig.
320 2a). For an open system with the exchange of matter and/or energy, the Gibbs energy of
321 the system deviates from the equilibrium G , G_{eq} (Fig. 4a). When Sp invades the system,
322 the utilization of Gibbs energy brings G closer to G_{eq} , establishing G_{bio} . Letting the
323 discrepancy between the steady-state G at the microbe-free state G_{bio}^* and G_{eq} be the
324 net available Gibbs energy ($G_{bio}^* - G_{eq}$), we can define the thermodynamic
325 efficiency of established pathways (η) as the ratio of the Gibbs energy utilized by the
326 microbial community ($G_{bio}^* - G_{bio}$) to the net available Gibbs energy: $\eta = (G_{bio}^* -$
327 $G_{bio}) / (G_{bio}^* - G_{eq})$.

328 When a monopoly Sp and mutualistic Sps are separately introduced to the
329 same microbe-free system, the Gibbs energy utilized by the monopoly Sp is often
330 greater than that utilized by either of the mutualistic Sps solely (Fig. 4a). However,
331 when both mutualistic Sps are present, they can efficiently utilize Gibbs energy by
332 enhancing material cycle and thus lower G where the monopoly Sp can no longer
333 survive (Fig. 4b). This relationship between G_{bio}^* and the competitive outcome is
334 similar to the R^* -rule stating that a species that can establish the lowest abundance of
335 resource at a steady state excludes others (Stewart & Levin 1973; Hsu *et al.* 1977;

336 Tilman 1977). Establishing pathways to better utilize the Gibbs energy would also be
337 related to the maximum power (entropy production) principle, which predicts the
338 direction of ecosystem development to maximize useful power (Odum & Pinkerton
339 1955; Nielsen *et al.* 2020). Figure 4c shows the Sp compositions that can establish the
340 lowest G_{bio}^* at a steady state explored by the simulations for all possible Sp
341 compositions. Monopoly Sp and mutualistic Sps competing for the same reaction niche
342 do not coexist, and whichever can minimize G_{bio}^* survives and excludes the other.
343 Meanwhile, Sps competing for the same reactant but not the same reaction niche can
344 coexist, and the Sp combination that minimizes G_{bio}^* is not always achieved. The
345 coexistence of competitive Sps often establishes higher G_{bio}^* than that established by
346 each Sp i alone because they inhibit each other's growth.

347 Mutualistic Sps driving a material cycle can outcompete monopoly Sp at a
348 larger inflow of X_j with well-balanced electron acceptors and donors. This leads to
349 higher thermodynamic efficiency and biomass productivity (Fig. 5a and b). Mutualistic
350 Sps also predominate when the catalytic abilities of all Sps are uniformly increased
351 (Fig. S1). This result supports the selective advantage for species that utilizes a reaction
352 with lower yield of ATP with a higher rate, even in the absence of the trade-off between
353 the yield and rate of ATP production. The thermodynamic efficiency decreases with the
354 increasing inflow rate of the most oxidized X_1 , although the net available Gibbs energy
355 ($G_{bio}^* - G_{eq}$) simultaneously increases. The decline in the thermodynamic efficiency
356 is attributable to a kinetic (or f_i -limiting) constraint on the utilization of the Gibbs
357 energy because of the resulting lack of electron donors. While the kinetic constraint
358 decreases the thermodynamic efficiency, in some cases it prevents the overuse of the

359 Gibbs energy by preventing the G_{bio}^* from getting too close to G_{eq} , where microbial
360 growth is self-regulated by the lack of energy, leading the lower biomass productivity.

361 For more complex networks, thermodynamic efficiency and total biomass can
362 simultaneously increase in response to the increase in the number of cycles and Sps
363 survived at a relatively lower inflow of X_j with a well-balanced supply of electron
364 donors and acceptors (Fig. 5c and d). The result implies that, at the redox boundary
365 under a limited supply of electron donors and acceptors, the species or functional
366 diversity of microbes can support the ecosystem productivity because the replacement
367 of monopolizing Sps by Sps with labor division leads to a more efficient use of the
368 Gibbs energy.

369

370 **Metabolic functional diversity and thermodynamic efficiency**

371 The complexity of the redox network template in this study is inextricably
372 linked to the diversity of microbial metabolic functions. As prokaryotes are thought to
373 have gradually become able to harness diverse chemical reactions during their evolution
374 (Nealson & Rye 2005), the redox network template would also have gradually become
375 more complex in response to microbial metabolic functional diversity. For any
376 thermodynamic and microbial conditions we explored, the increase in the complexity of
377 the network template, characterized by the number of X_j participating in redox reactions
378 N_{tot} , favors pathways that incorporate more cyclic structures with smaller ρ_i . This leads
379 to higher thermodynamic efficiency and biomass productivity (Figs. 6). Sps with higher
380 r_i and lower K_{i,X_j} were selected within a more complex network template because of
381 the intensive competition. The established pathways incorporate more cycles than those
382 established by Sps with constant r_i and K_{i,X_j} (cf. Figs. 6 and S2), which implies that

383 not only the metabolic diversity for the energy source but also the difference in
384 microbial catalytic abilities can enhance the division of labor that drives material cycles.

385

386 **Discussion**

387 Microbial life in a system with low energy supply has been considered to
388 employ two strategies for energy utilization. The first is energy conservation at an
389 individual level by lowering maintenance costs (Hoehler & Jørgensen 2013b; Lever *et al.*
390 *al.* 2015), while the second is energy use optimization by differentiating metabolic
391 pathways depending on the resource influx (Pfeiffer *et al.* 2001; Kreft *et al.* 2020).

392 Here, we propose a new strategy, an energy efficiency strategy at the community level:
393 microbial metabolic diversity can increase power generation through the enhancement
394 of division of labor, which accelerates material cycling through complex community
395 interactions, especially at redox boundaries where both electron donors and acceptors
396 are supplied in a balanced way.

397 Furthermore, our findings explain the ecological advantage of species using
398 reactions with low $-\Delta_rG$. These species appear to be tolerating the energetically harsh
399 environments, but can significantly impact on their ecosystem, like a keystone species.
400 Examples may include bacterial species harnessing nitrite oxidation with relatively
401 lower $-\Delta_rG$ (or lower ρ) in the nitrogen cycle. Nitrification occurs in two consecutive
402 steps (ammonia oxidation to nitrite and nitrite oxidation to nitrate) or in the complete
403 ammonia oxidation to nitrate (Daims *et al.* 2015). The advantage of nitrite oxidation has
404 often been discussed in terms of the competition with complete ammonia oxidation
405 (Costa *et al.* 2006); however, our study suggests that the survival strategy of nitrite-

406 oxidizing bacteria is rather to function as a key cog to form subcycles with nitrate
407 oxidation or denitrification.

408 The thermodynamic efficiency and the total biomass increased markedly with
409 an increase in metabolic diversity, especially when the supply of electron donors and
410 acceptors were balanced (Fig. 6b). This may be associated with the time interval
411 between the evolution of oxygenic photosynthetic organisms and the Great Oxidation
412 Event (GOE). Although the GOE is generally accepted to have been driven by the
413 evolution of oxygenic photosynthesis, oxygenic photosynthesis is thought to have
414 evolved a few hundred million to a few billion years before GOE (Planavsky *et al.*
415 2014; Ward *et al.* 2016). This time interval has traditionally been associated with
416 geological O₂ sinks, and a recent study suggested that the competitive outcome
417 between oxygenic and anoxygenic photosynthetic organisms may have contributed to
418 the timing of the GOE (Olejarz *et al.* 2021). Our study indicates that chemotrophic
419 communities may have served as missing sinks for O₂ as the increase in oxygen in the
420 relatively reduced atmosphere may have reached a quantity sufficient to drive redox
421 cycles, enabling chemotrophic microbial communities to proliferate. If microbial
422 metabolic diversity increases simultaneously, more oxygen could have been utilized
423 because of the enhanced thermodynamic efficiency and the productivity.

424 This study did not delve into the relationship between the thermodynamic
425 efficiency and the robustness of a microbial community. We confirmed the presence of
426 multistable steady states (see Section S3), each characterized by different species
427 compositions with different thermodynamic efficiencies. Intuitively, more productive
428 microbial communities with higher species diversity (or functional diversity) would be
429 robust to environmental disturbances. Furthermore, the microbial ecosystem

430 productivity would be maintained by the plastic responses of metabolic pathways (or
431 species composition) that enable microbial communities to utilize the Gibbs energy at a
432 reasonable thermodynamic efficiency.

433 The energy efficiency strategy at the community level is supported by the
434 functional segmentation and differentiation of a microbial module, which would be
435 particularly advantageous in fluctuating environments. However, in relatively stable
436 environments, the shape of microbial metabolic pathways and species composition
437 would also be stably maintained. The more constant and intimate interspecific
438 interactions among unicellular cells in a consortium may have facilitated the
439 evolutionary transition to a unicellular cell with more complex metabolic functions,
440 such as aerobic respiration, and then eventually to a multicellular organism.

441

442 **Acknowledgements**

443 This study was supported by JSPS Grant-in-Aid for Scientific Research (C)
444 Grant Numbers 19K06853 and 22K06390 (to MS) and by JSPS KAKENHI
445 (JP19H05641 and JP21H05315) and the Environment Research and Technology
446 Development Fund (JPMEERF20214103) of the Environmental Restoration and
447 Conservation Agency of Japan (to MK). We thank the following people for their
448 comments: Y. Iwasa, K. Kadowaki, and Y. Tachiki.

449

450

451 **References**

452 Anantharaman, K., Brown, C.T., Hug, L.A., Sharon, I., Castelle, C.J., Probst, A.J., *et al.*

453 (2016). Thousands of microbial genomes shed light on interconnected
454 biogeochemical processes in an aquifer system. *Nature Communications*, 7.

455 Bar-On, Y.M., Phillips, R. & Milo, R. (2018). The biomass distribution on Earth.
456 *Proceedings of the National Academy of Sciences*, 115, 6506–6511.

457 Boetius, A., Ravenschlag, K., Schubert, C.J., Rickert, D., Widdel, F., Gieseke, A., *et al.*
458 (2000). A marine microbial consortium apparently mediating anaerobic oxidation
459 of methane. *Nature*, 407, 623–626.

460 Bradley, J.A., Arndt, S., Amend, J.P., Burwicz, E., Dale, A.W., Egger, M., *et al.* (2020).
461 Widespread energy limitation to life in global subseafloor sediments. *Science*
462 *Advances*, 6, 1–9.

463 Bryant, M.P., Wolin, E.A., Wolin, M.J. & Wolfe, R.S. (1967). Methanobacillus
464 omelianskii, a symbiotic association of two species of bacteria., 59, 20–31.

465 Costa, E., Pérez, J. & Kreft, J.U. (2006). Why is metabolic labour divided in
466 nitrification? *Trends in Microbiology*, 14, 213–219.

467 Daims, H., Lebedeva, E. V., Pjevac, P., Han, P., Herbold, C., Albertsen, M., *et al.*
468 (2015). Complete nitrification by Nitrospira bacteria. *Nature*, 528, 504–509.

469 Embree, M., Liu, J.K., Al-Bassam, M.M. & Zengler, K. (2015). Networks of energetic
470 and metabolic interactions define dynamics in microbial communities. *Proceedings*
471 *of the National Academy of Sciences of the United States of America*, 112, 15450–
472 15455.

473 Falkowski, P.G., Fenchel, T. & Delong, E.F. (2008). The microbial engines that drive
474 Earth's biogeochemical cycles. *Science*, 320, 1034–1039.

475 Flemming, H.C. & Wuertz, S. (2019). Bacteria and archaea on Earth and their
476 abundance in biofilms. *Nature Reviews Microbiology*, 17, 247–260.

477 Hoehler, T.M., Alperin, M.J., Albert, D.B. & Martens, C.S. (1994). Field and laboratory
478 studies of methane oxidation in an anoxic marine sediment: Evidence for a
479 methanogen-sulfate reducer consortium. *Global Biogeochemical Cycles*, 8, 878–
480 879.

481 Hoehler, T.M. & Jørgensen, B.B. (2013a). Microbial life under extreme energy
482 limitation. *Nat. Rev. Microbiol.*, 11, 83–94.

483 Hoehler, T.M. & Jørgensen, B.B. (2013b). Microbial life under extreme energy
484 limitation. *Nature Reviews Microbiology*.

485 Hsu, S.B., Hubble, S. & Waitman, P. (1977). A mathematical theory of single-nutrient
486 competition in continuous cultures of micro-organisms. *SIAM J. Appl. Math.*, 32,
487 366–383.

488 Jørgensen, B.B. & Boetius, A. (2007). Feast and famine - Microbial life in the deep-sea
489 bed. *Nature Reviews Microbiology*, 5, 770–781.

490 Kallmeyer, J., Pockalny, R., Adhikari, R.R., Smith, D.C. & D’Hondt, S. (2012). Global
491 distribution of microbial abundance and biomass in subseafloor sediment.
492 *Proceedings of the National Academy of Sciences of the United States of America*,
493 109, 16213–16216.

494 Kouzuma, A., Kato, S. & Watanabe, K. (2015). Microbial interspecies interactions:
495 Recent findings in syntrophic consortia. *Frontiers in Microbiology*.

496 Kreft, J.U., Griffin, B.M. & González-Cabaleiro, R. (2020). Evolutionary causes and
497 consequences of metabolic division of labour: why anaerobes do and aerobes
498 don’t. *Current Opinion in Biotechnology*.

499 Kuypers, M.M.M., Marchant, H.K. & Kartal, B. (2018). The microbial nitrogen-cycling
500 network. *Nature Reviews Microbiology*.

501 Lever, M.A., Rogers, K.L., Lloyd, K.G., Overmann, J., Schink, B., Thauer, R.K., *et al.*
502 (2015). Life under extreme energy limitation: A synthesis of laboratory- and field-
503 based investigations. *FEMS Microbiology Reviews*.

504 Magnabosco, C., Lin, L.H., Dong, H., Bomberg, M., Ghiorse, W., Stan-Lotter, H., *et al.*
505 (2018). The biomass and biodiversity of the continental subsurface. *Nature*
506 *Geoscience*, 11, 707–717.

507 McInerney, M.J., Sieber, J.R. & Gunsalus, R.P. (2009). Syntrophy in anaerobic global
508 carbon cycles. *Current Opinion in Biotechnology*, 20, 623–632.

509 Momper, L., Jungbluth, S.P., Lee, M.D. & Amend, J.P. (2017). Energy and carbon
510 metabolisms in a deep terrestrial subsurface fluid microbial community. *ISME*
511 *Journal*, 11, 2319–2333.

512 Morono, Y., Terada, T., Nishizawa, M., Ito, M., Hillion, F., Takahata, N., *et al.* (2011).
513 Carbon and nitrogen assimilation in deep subseafloor microbial cells. *Proceedings*
514 *of the National Academy of Sciences*, 201107763.

515 Morris, B.E.L., Henneberger, R., Huber, H. & Moissl-Eichinger, C. (2013). Microbial
516 syntrophy: Interaction for the common good. *FEMS Microbiology Reviews*, 37,

517 384–406.

518 Neilson, K.H. & Rye, R. (2005). *Evolution of Metabolism. Biogeochemistry* (ed. W.H.

519 Schlesinger) *Vol.8 Treatise on Geochemistry* (eds. H.D. Holland and K.K.

520 Turekian). Elsevier-Pergamon, Oxford.

521 Nielsen, S.N., Müller, F., Marques, J.C., Bastianoni, S. & Jørgensen, S.E. (2020).

522 Thermodynamics in ecology-An introductory review. *Entropy*, 22.

523 Odum, H.T. & Pinkerton, R.C. (1955). Time's speed regulator: the optimum efficiency

524 for maximum power output in physical and biological systems. *American Scientist*,

525 43.

526 Olejarz, J., Iwasa, Y., Knoll, A.H. & Nowak, M.A. (2021). The Great Oxygenation

527 Event as a consequence of ecological dynamics modulated by planetary change.

528 *Nature Communications*, 12.

529 Pfeiffer, T., Schuster, S. & Bonhoeffer, S. (2001). Cooperation and competition in the

530 evolution of ATP-producing pathways. *Science*, 292, 504–507.

531 Planavsky, N.J., Asael, D., Hofmann, A., Reinhard, C.T., Lalonde, S. V., Knudsen, A.,

532 *et al.* (2014). Evidence for oxygenic photosynthesis half a billion years before the

533 Great Oxidation Event. *Nature Geoscience*, 7.

534 Roden, E.E., Sobolev, D., Glazer, B. & Luther, G.W. (2004). Potential for Microscale
535 Bacterial Fe Redox Cycling at the Aerobic-Anaerobic Interface. *Geomicrobiology*
536 *Journal*, 21, 379–391.

537 Seto, M. & Iwasa, Y. (2019a). Population dynamics of chemotrophs in anaerobic
538 conditions where the metabolic energy acquisition per redox reaction is limited.
539 *Journal of Theoretical Biology*, 467.

540 Seto, M. & Iwasa, Y. (2019b). The fitness of chemotrophs increases when their
541 catabolic by-products are consumed by other species. *Ecology Letters*, 22, 1994–
542 2005.

543 Seto, M. & Iwasa, Y. (2020). Microbial material cycling, energetic constraints and
544 ecosystem expansion in subsurface ecosystems. *Proceedings of the Royal Society*
545 *B: Biological Sciences*, 287, 20200610.

546 Starnawski, P., Bataillon, T., Ettema, T.J.G., Jochum, L.M., Schreiber, L., Chen, X., *et*
547 *al.* (2017). Microbial community assembly and evolution in subseafloor sediment.
548 *Proceedings of the National Academy of Sciences of the United States of America*,

549 201614190.

550 Stewart, F.M. & Levin, B.R. (1973). Partitioning of Resources and the Outcome of
551 Interspecific Competition: A Model and Some General Considerations. *The*
552 *American Naturalist*, 107, 171–198.

553 Tilman, D. (1977). Resource Competition between planktonic algae: an experimental
554 and theoretical approach. *Ecology*, 58, 338–348.

555 Ward, L.M., Kirschvink, J.L. & Fischer, W.W. (2016). Timescales of Oxygenation
556 Following the Evolution of Oxygenic Photosynthesis. *Origins of Life and*
557 *Evolution of Biospheres*, 46.

558 Zerkle, A.L. & Mikhail, S. (2017). The geobiological nitrogen cycle: From microbes to
559 the mantle. *Geobiology*, 15.

560

561 **Figure legends**

562 **Fig. 1 | Outline of the eco-redox model. a.** The redox network template and its
563 material network when $(N_A, N_B, N_C) = (2, 2, 2)$ and $(N_A, N_B, N_C) = (4, 4, 4)$. i in the
564 smaller nodes denotes the energy-source reaction for Sp i . Blue and red arrows
565 correspond to oxidation and reduction reactions, respectively (solid for reaction 1 and
566 dotted for reaction 4, the reverse reaction of reaction 1). **b.** Thermodynamic advantage

567 of the i th reaction weighted by the negative of the Gibbs energy change of reaction ($-\Delta_r G_i$). **c.** Microbially established pathways at a steady state within the same redox network template composed of X_j with different standard chemical potentials. For **b** and **c**, the sizes of the nodes are weighted by the chemical potential of X_j at a steady state.

571

572 **Fig. 2 | Division of labor within a redox network. a.** Interspecific relationships among
573 three Sps and the competitive relationship between Sps with labor division and Sp using
574 a complete reaction within the redox network template at $(N_A, N_B, N_C) = (2, 2, 2)$. **b.**
575 Examples of complex division of labor and the degree of segmentation of the i th redox
576 reaction, $\rho_i = -\Delta_r G_i / \max. (-\Delta_r G_1, \dots, -\Delta_r G_{N_{\text{reac}}})$. **c.** An example of the dynamics within
577 a redox template consisting of 60 reactions and the same number of Sps at (N_A, N_B, N_C)
578 $= (3, 3, 3)$. The edges in the upper and lower network diagrams are weighted by the
579 degree of segmentation and the flow rate $(f_i M_i + F_i)$ at $t = 0, 10, \text{ and } 2000$, respectively.
580 The nodes representing X_j are weighted by the chemical potential of X_j at each t . The
581 table summarizes the values of $-\Delta_r G_i$ and ρ_i of the microbial pathways established at a
582 steady state. **d.** The dynamics when each of the Sps that survived at the steady state in **c**
583 was consecutively introduced to a microbe-free system. The nodes representing X_j are
584 weighted by the chemical potential of X_j at a steady state. The values of the
585 thermodynamic, kinetic, and microbial parameters used for **c** are provided in csv files
586 along with a sample program written in Wolfram language (see Supporting Information
587 S2.2).

588

589 **Fig. 3 | Establishment of cyclic pathways and division of labor at a steady state at**

590 $(N_A, N_B, N_C) = (4, 4, 4)$. **a.** Average number of cycles established in response to the
591 change in the inflow rate of all X_j ($I_{X_j} = [\text{Inflow rate}]/N_{tot}$ shown by solid lines) and
592 only the most oxidized X_1 ($I_{X_1} = [\text{Inflow rate}]$ and 10^{-5} for other I_{X_j} shown by
593 dotted lines), respectively, with 1000 iterations for each inflow rate. **b** Number of
594 established cycles at various redox balances when the values of I_{X_j} were randomly
595 selected at a fixed total inflow rate ($\sum_X \sum_j I_{X_j} = 10^{-3}$), with 5000 iterations. The redox
596 balance of the inflow was estimated by balancing the abundance of electron acceptors
597 and donors in the inflow. **c.** Probability of the established pathways possessing no cycles
598 and four cycles at varying I_{X_j} , with 20000 iterations. **d.** Average of the number of Sps
599 (left) and the minimum of ρ_i (right) of the established pathways with x cycles to the
600 change in the inflow rate of all X_j ($I_{X_j} = [\text{Inflow rate}]/N_{tot}$), with 1000 iterations for
601 each inflow rate. The values of other parameters and ranges for random variables are
602 summarized in Table S1. The error bars show 2 SE in **a** and **d** and the maximum and
603 minimum values in **b**.

604
605 **Fig. 4 | Competitive outcome between a monopolizing Sp (Sp 1) and mutualistic**
606 **Sps with labor division (Sps 2 and 3) and the utilization of Gibbs energy at $(N_A, N_B,$**
607 **$N_C) = (2, 2, 2)$. **a.** Dynamics of microbial growth (top left and right), Gibbs energy G**
608 **(down left), and thermodynamic efficiency η (down right) when a monopoly Sp was**
609 **solely (top left) and mutualistic Sps were sequentially (top right) introduced to the same**
610 **microbe-free environment. There were no inflow and outflow at $0 \leq t < 1000$. **b.****
611 **Dynamics of microbial growth when Sps 1-3 were introduced to the microbe-free**
612 **system at $t = 0$. **c.** Combination of Sps that established the lowest G_{bio}^* (left) and Sps**

613 that survived at a steady state (right) in response to the change in the inflow rates of B₁
614 and B₂. The parameters and initial values are shown in Table S2.

615

616 **Fig. 5 | Steady-state total biomass and thermodynamic efficiency in response to the**

617 **inflow rate of X_j at (N_A, N_B, N_C) = (2, 2, 2) (a, b) and at (N_A, N_B, N_C) = (4, 4, 4) (c,**

618 **d). a.** The responses of the types of interspecific relationships (top), thermodynamic

619 efficiency (middle), and total biomass (bottom) to the change in the inflow rate of all X_j

620 ($I_{X_j} = [\text{Inflow rate}]/N_{tot}$) (left) and only the most oxidized X₁ ($I_{X_1} = [\text{Inflow rate}]$

621 and 10^{-5} for other I_{X_j}) (right). **b.** The relationship between the total biomass and

622 thermodynamic efficiency at $I_{X_j} = 10^{-6}/6$ for all X_j. For **a** and **b**, black, red, and blue

623 show the steady state where monopoly Sp only exists, competitive two Sps coexist, and

624 mutualistic two Sps coexist, respectively. **c.** The responses of the thermodynamic

625 efficiency (top) and total biomass (bottom) to the change in the inflow rate of all X_j

626 ($I_{X_j} = [\text{Inflow rate}]/N_{tot}$ shown by solid lines) and only the most oxidised X₁ ($I_{X_1} =$

627 $[\text{Inflow rate}]$ and 10^{-5} for other I_{X_j} shown by dotted lines). **d.** Relationships between

628 the thermodynamic efficiency and the number of Sps (top left), the thermodynamic

629 efficiency and the number of cycles (top right), the total biomass normalized by the total

630 inflow rate ($\sum_i M_i^* / \sum_X \sum_j I_{X_j}$) and the number of Sps (bottom left), and the total

631 biomass normalized by the total inflow rate and the number of cycles (bottom right) at

632 different inflow rate (I_{X_j}) of all X_j. Other parameters were set to the default values

633 shown in Table S1. The simulation was iterated 1000 times for each inflow rate. The

634 error bars show 2 SE.

635

636

637 **Fig. 6 | Steady-state responses to changes in the inflow rate and the redox network**
638 **template complexity as microbial functional complexity. a, b.** Steady-state responses
639 at different inflow rates of all X_j ($I_{X_j} = [\text{Inflow rate}]/N_{tot}$) (**a**) and only the most
640 oxidised X_1 ($I_{X_1} = [\text{Inflow rate}]$ and 10^{-5} for other I_{X_j}) (**b**) at different levels of the
641 redox network template complexity characterized by the total number of X-bearing
642 chemical species (N_{tot}) utilized by microbes. (Top left) Average of the number of cycles;
643 (top right) the minimum degree of segmentation; (middle left) thermodynamic
644 efficiency; (middle right) total biomass normalized by the total inflow rate
645 ($\sum_i M_i^* / \sum_X \sum_j I_{X_j}$); (bottom left and right) microbial catalytic rate and Michaelis-
646 Menten constant of Sps survived at steady state. For **b**, the redox condition of inflow is
647 the most balanced at $\log_{10} I_{X_j} = -5$. The simulations at a given inflow rate and N_{tot}
648 condition were repeated 1000 times. Other parameters were set to the default values
649 shown in Table S1.

650

651 **Competing interests**

652 The authors declare no competing interests.

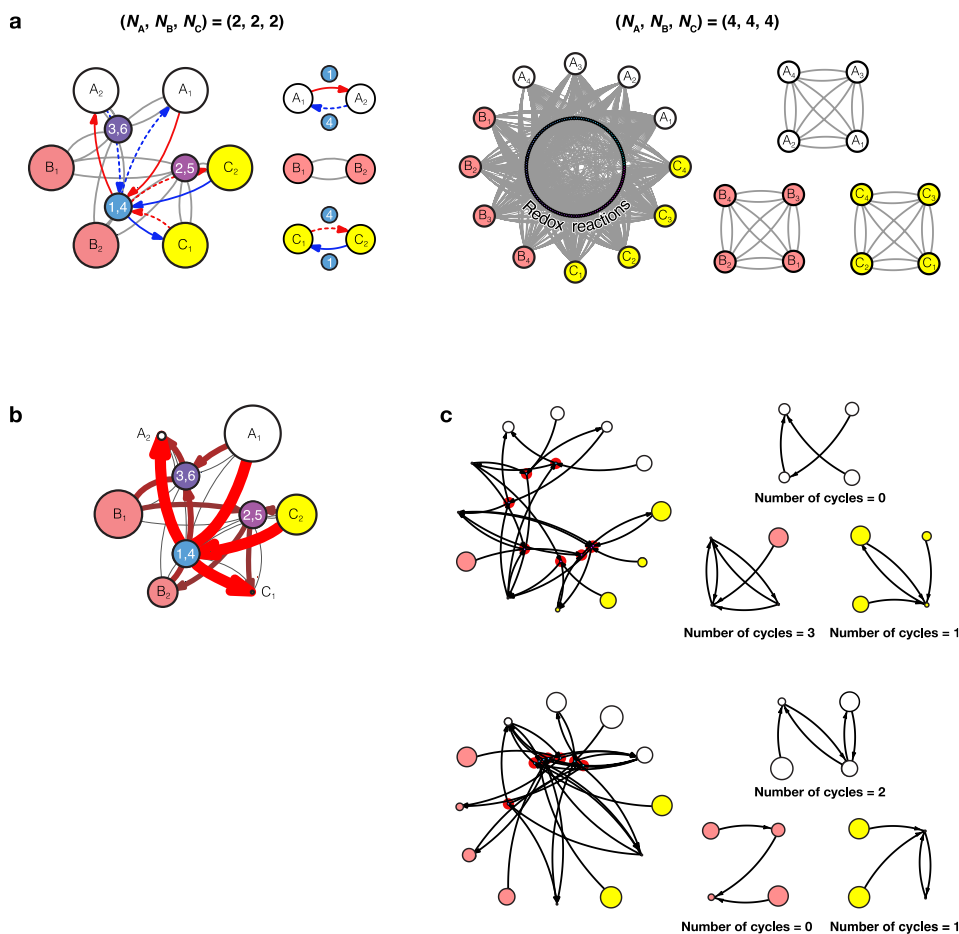
653

654 **Supplementary Information** is available for this paper.

655

656 **Correspondence and requests for materials should be addressed to Mayumi Seto**

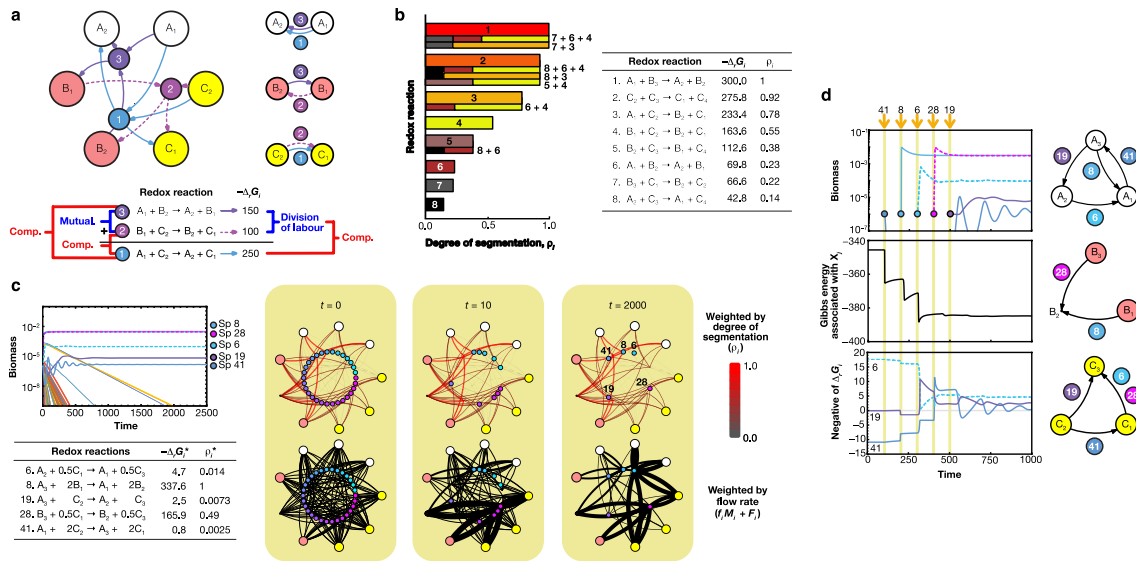
657



660

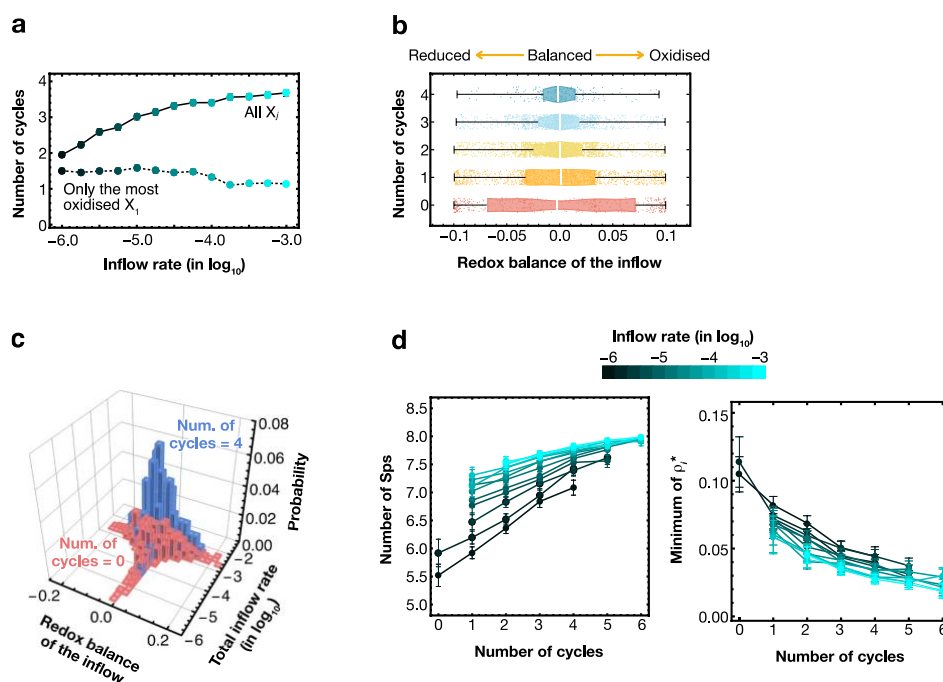
661 **Fig. 1 | Outline of the eco-redox model. a.** The redox network template and its
 662 material network when $(N_A, N_B, N_C) = (2, 2, 2)$ and $(N_A, N_B, N_C) = (4, 4, 4)$. i in the
 663 smaller nodes denotes the energy-source reaction for Sp i . Blue and red arrows
 664 correspond to oxidation and reduction reactions, respectively (solid for reaction 1 and
 665 dotted for reaction 4, the reverse reaction of reaction 1). **b.** Thermodynamic advantage
 666 of the i th reaction weighted by the negative of the Gibbs energy change of reaction ($-\Delta_r G_i$). **c.** Microbially established pathways at a steady state within the same redox
 667 network template composed of X_j with different standard chemical potentials. For **b** and
 668 **c**, the sizes of the nodes are weighted by the chemical potential of X_j at a steady state.
 669

670



671

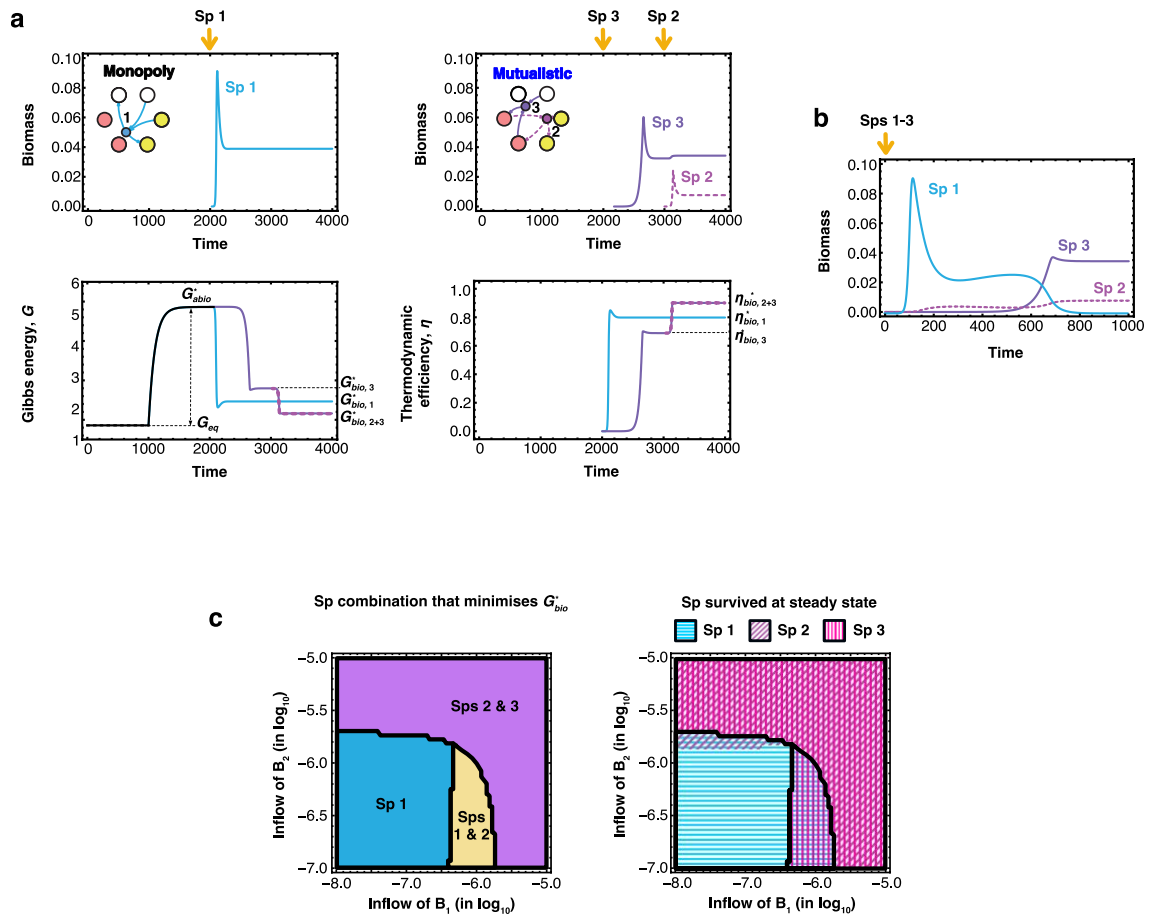
672 **Fig. 2 | Division of labor within a redox network.** **a.** Interspecific relationships among
673 three Sps and the competitive relationship between Sps with labor division and Sp using
674 a complete reaction within the redox network template at $(N_A, N_B, N_C) = (2, 2, 2)$. **b.**
675 Examples of complex division of labor and the degree of segmentation of the i th redox
676 reaction, $\rho_i = -\Delta_r G_i / \max. (-\Delta_r G_1, \dots, -\Delta_r G_{N_{\text{reac}}})$. **c.** An example of the dynamics within
677 a redox template consisting of 60 reactions and the same number of Sps at (N_A, N_B, N_C)
678 $= (3, 3, 3)$. The edges in the upper and lower network diagrams are weighted by the
679 degree of segmentation and the flow rate $(f_i M_i + F_i)$ at $t = 0, 10$, and 2000 , respectively.
680 The nodes representing X_j are weighted by the chemical potential of X_j at each t . The
681 table summarizes the values of $-\Delta_r G_i$ and ρ_i of the microbial pathways established at a
682 steady state. **d.** The dynamics when each of the Sps that survived at the steady state in **c**
683 was consecutively introduced to a microbe-free system. The nodes representing X_j are
684 weighted by the chemical potential of X_j at a steady state. The values of the
685 thermodynamic, kinetic, and microbial parameters used for **c** are provided in csv files
686 along with a sample program written in Wolfram language (see Supporting Information
687 S2.2).
688



689

690

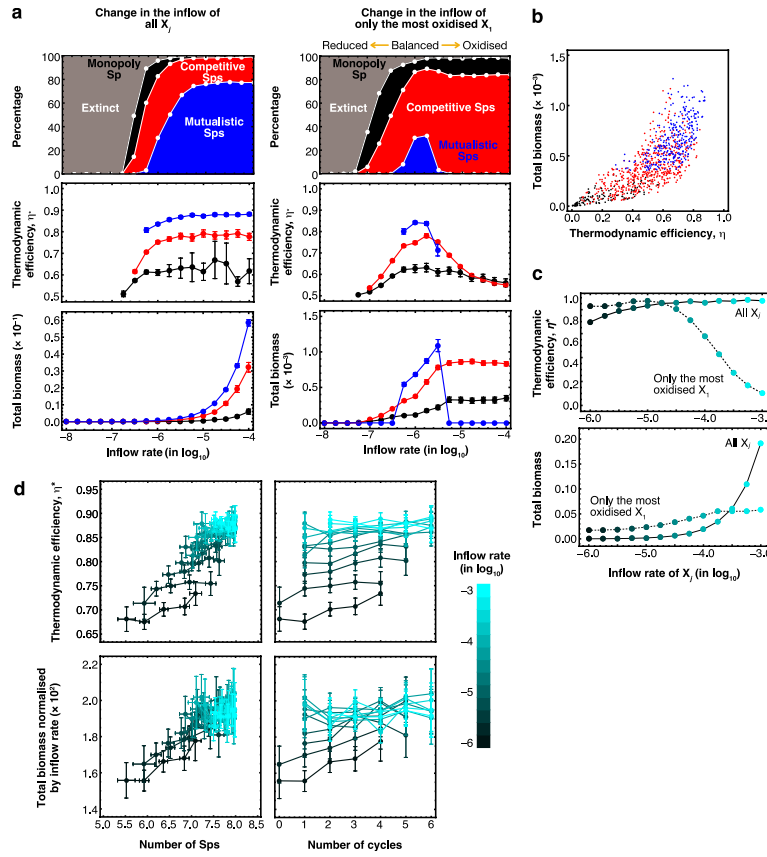
691 **Fig. 3 | Establishment of cyclic pathways and division of labor at a steady state at**
 692 **$(N_A, N_B, N_C) = (4, 4, 4)$.** **a.** Average number of cycles established in response to the
 693 change in the inflow rate of all X_j ($I_{X_j} = [\text{Inflow rate}]/N_{tot}$ shown by solid lines) and
 694 only the most oxidized X_1 ($I_{X_1} = [\text{Inflow rate}]$ and 10^{-5} for other I_{X_j} shown by
 695 dotted lines), respectively, with 1000 iterations for each inflow rate. **b** Number of
 696 established cycles at various redox balances when the values of I_{X_j} were randomly
 697 selected at a fixed total inflow rate ($\sum_X \sum_j I_{X_j} = 10^{-3}$), with 5000 iterations. The redox
 698 balance of the inflow was estimated by balancing the abundance of electron acceptors
 699 and donors in the inflow. **c.** Probability of the established pathways possessing no cycles and
 700 four cycles at varying I_{X_j} , with 20000 iterations. **d.** Average of the number of Sps
 701 (left) and the minimum of ρ_i (right) of the established pathways with x cycles to the
 702 change in the inflow rate of all X_j ($I_{X_j} = [\text{Inflow rate}]/N_{tot}$), with 1000 iterations for
 703 each inflow rate. The values of other parameters and ranges for random variables are
 704 summarized in Table S1. The error bars show 2 SE in **a** and **d** and the maximum and
 705 minimum values in **b**.
 706



707

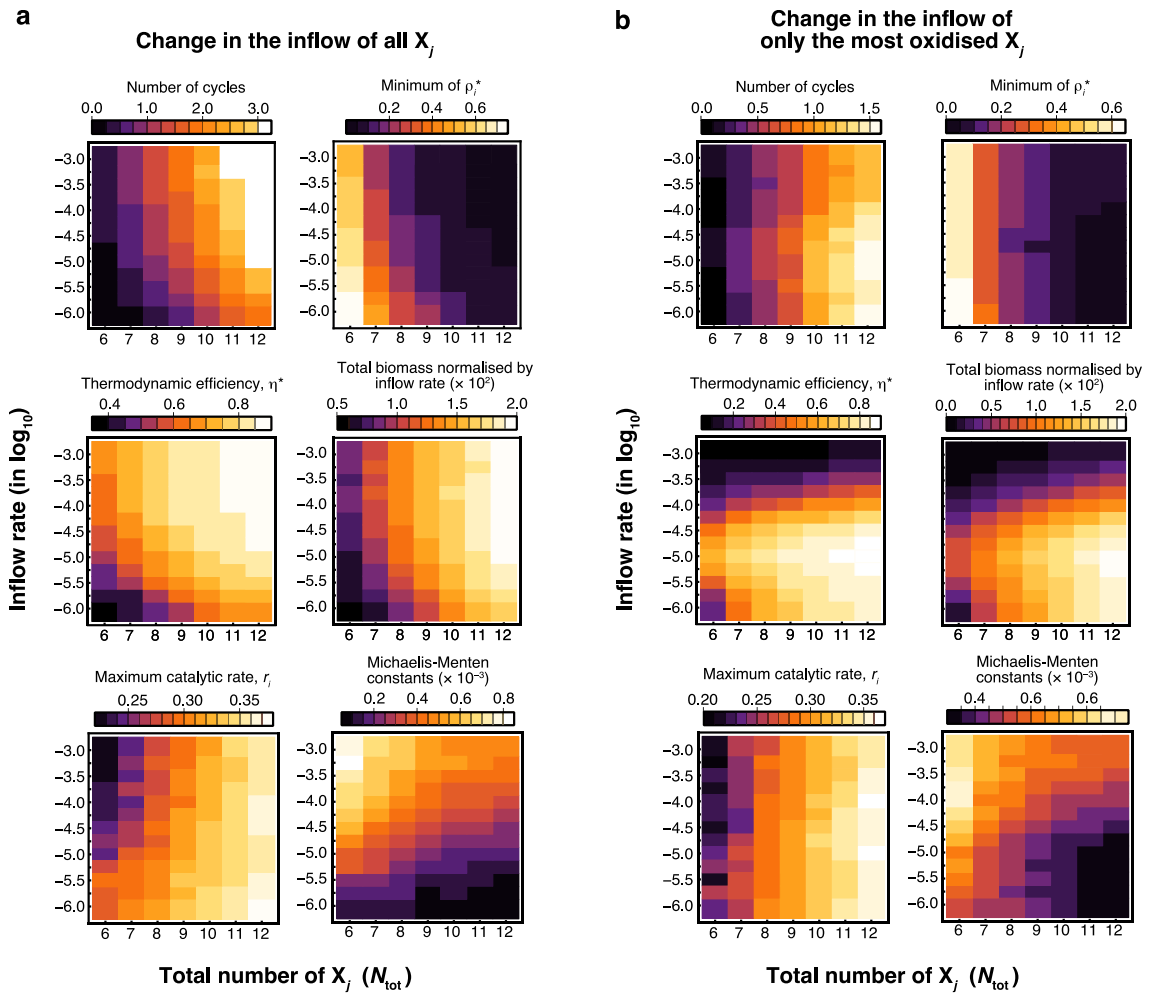
708 **Fig. 4 | Competitive outcome between a monopolizing Sp (Sp 1) and mutualistic**
 709 **Sps with labor division (Sps 2 and 3) and the utilization of Gibbs energy at $(N_A, N_B,$**
 710 **$N_C) = (2, 2, 2)$. **a.** Dynamics of microbial growth (top left and right), Gibbs energy G**
 711 **(down left), and thermodynamic efficiency η (down right) when a monopoly Sp was**
 712 **solely (top left) and mutualistic Sps were sequentially (top right) introduced to the same**
 713 **microbe-free environment. There were no inflow and outflow at $0 \leq t < 1000$. **b.****
 714 **Dynamics of microbial growth when Sps 1-3 were introduced to the microbe-free**
 715 **system at $t = 0$. **c.** Combination of Sps that established the lowest G_{bio}^* (left) and Sps**
 716 **that survived at a steady state (right) in response to the change in the inflow rates of B_1**
 717 **and B_2 . The parameters and initial values are shown in Table S2.**

718



719

720 **Fig. 5 | Steady-state total biomass and thermodynamic efficiency in response to the**
721 **inflow rate of X_j at $(N_A, N_B, N_C) = (2, 2, 2)$ (a, b) and at $(N_A, N_B, N_C) = (4, 4, 4)$ (c,**
722 **d). a.** The responses of the types of interspecific relationships (top), thermodynamic
723 efficiency (middle), and total biomass (bottom) to the change in the inflow rate of all X_j
724 ($I_{X_j} = [\text{Inflow rate}]/N_{tot}$) (left) and only the most oxidized X_1 ($I_{X_1} = [\text{Inflow rate}]$ and
725 10^{-5} for other I_{X_j}) (right). **b.** The relationship between the total biomass and
726 thermodynamic efficiency at $I_{X_j} = 10^{-6}/6$ for all X_j . For **a** and **b**, black, red, and blue
727 show the steady state where monopoly Sp only exists, competitive two Sps coexist, and
728 mutualistic two Sps coexist, respectively. **c.** The responses of the thermodynamic
729 efficiency (top) and total biomass (bottom) to the change in the inflow rate of all X_j
730 ($I_{X_j} = [\text{Inflow rate}]/N_{tot}$ shown by solid lines) and only the most oxidized X_1 ($I_{X_j} =$
731 $[\text{Inflow rate}]/N_{tot}$). **d.** Relationships between the thermodynamic efficiency and the
732 number of Sps (top left), the thermodynamic efficiency and the number of cycles (top
733 right), the total biomass normalized by the total inflow rate ($\sum_i M_i^* / \sum_X \sum_j I_{X_j}$) and the
734 number of Sps (bottom left), and the total biomass normalized by the total inflow rate
735 and the number of cycles (bottom right) at different inflow rate (I_{X_j}) of all X_j . Other
736 parameters were set to the default values shown in Table S1. The simulation was
737 iterated 1000 times for each inflow rate. The error bars show 2 SE.



738

739

740 **Fig. 6 | Steady-state responses to changes in the inflow rate and the redox network**
 741 **template complexity as microbial functional complexity. a, b.** Steady-state responses

742 at different inflow rates of all X_j ($I_{X_j} = [\text{Inflow rate}]/N_{tot}$) (a) and only the most

743 oxidised X_1 ($I_{X_1} = [\text{Inflow rate}]$ and 10^{-5} for other I_{X_j}) (b) at different levels of the

744 redox network template complexity characterized by the total number of X-bearing

745 chemical species (N_{tot}) utilized by microbes. (Top left) Average of the number of cycles;

746 (top right) the minimum degree of segmentation; (middle left) thermodynamic

747 efficiency; (middle right) total biomass normalized by the total inflow rate

748 ($\sum_i M_i^* / \sum_X \sum_j I_{X_j}$); (bottom left and right) microbial catalytic rate and Michaelis-

749 Menten constant of Sps survived at steady state. For b, the redox condition of inflow is

750 the most balanced at $\log_{10} I_{X_j} = -5$. The simulations at a given inflow rate and N_{tot}

751 condition were repeated 1000 times. Other parameters were set to the default values

752

753